



Article

New Insights for Understanding the Structural Deformation Style of the Strike-Slip Regime along the Wadi Shueib and Amman-Hallabat Structures in Jordan Based on Remote Sensing Data Analysis

Mu'ayyad Al Hseinat ^{1,*} , Abdulla Al-Rawabdeh ^{2,*} , Malek Al-Zidaneen ¹, Hind Ghanem ¹, Masdouq Al-Taj ³, Abdullah Diabat ⁴, Ghaleb Jarrar ¹ and Mohammad Atallah ²

¹ Department of Geology, The University of Jordan, Amman 11942, Jordan; malek.soudi@gmail.com (M.A.-Z.); h.ghanem@ju.edu.jo (H.G.); jarrargh@ju.edu.jo (G.J.)

² Department of Earth and Environmental Sciences, Applied Geoinformatics Laboratory, Yarmouk University, Irbid 21163, Jordan; matallah@yu.edu.jo

³ Faculty of Natural Resources and Environment, Hashemite University, Zarqa 13133, Jordan; maltaj@hu.edu.jo

⁴ Institute of Earth and Environmental Sciences, Al al-Bayt University, Mafraq 25113, Jordan; adiatat@aabu.edu.jo

* Correspondence: m.hseinat@ju.edu.jo (M.A.H.); abd_rawabdeh@yu.edu.jo (A.A.-R.); Tel.: +962-6-5355000 (ext. 22262) (M.A.H.); +962-2-7211111 (ext. 2929) (A.A.-R.)

Received: 12 May 2020; Accepted: 29 June 2020; Published: 2 July 2020



Abstract: This paper presents new findings that contribute to the understanding of the deformational style of the Wadi Shueib Structure (WSS) and the Amman-Halabat Structure (AHS) and their relationship with the regional tectonic regime of the Dead Sea Transform Fault (DSTF). Our research utilized Landsat-8 OLI imagery for the automatic extraction of lineaments, and our lineament mapping was facilitated by processing and digital image enhancement using principal component analysis (PCA). Our data revealed a relatively higher density of lineaments along the extension of the major faults of the WSS and AHS. However, a relatively lower density of lineaments was shown in areas covered by recent deposits. Two major lineament trends were observed (NNE-SSW and NW-SE) in addition to a minor one (NE-SW), and most of these lineaments are parallel to the orientation of the WSS and AHS. We offer the supposition that the DSTF has merged into the major faults of the WSS and AHS. We further suppose that these faults were reactivated as a restraining bend composed of active strike-slip fault branches that developed due to the NNW-SSE-trending Dead Sea transpressional stress field. Depending on the relationship between the direction of the WSF and AHF strands and the regional tectonic displacement along the DSTF, thrust components are present on faults with horsetail geometry, and these movements are accompanied by folding and uplifting. Thus, the major faults of the WSS and AHS represent a contractional horsetail geometry with associated folding and thrusting deformation.

Keywords: Dead Sea Transform Fault (DSTF); Wadi Shueib Structure (WSS); Amman-Hallabat Structure (AHS); horsetail geometry; lineaments; remote sensing

1. Introduction

Strike-slip movement is a common process of deformation in both the continental and oceanic crust that exists at a wide range of scales. Several structural features have been recognized within/around strike-slip fault systems, such as horsetail structures (e.g., [1–9]). These structures tend to develop

where slip dies out more gradually towards the fault tip [10] and are used to describe the characteristic strike-slip fault and its deformation pattern [8]. Several previous studies on the strike-slip mechanism focused on the development of horsetail structures in shear zones and were interpreted by the simple shear model [1,2,4]. More recent studies interpreted these structures by the transpression/transension model (e.g., [3,11,12]). The simple shear model was utilized in the study area of our research.

The study area is ~1970 km² and extends to the east of the Dead Sea Transform Fault (DSTF) in the Jordan Valley, covering the area around the Wadi Shueib Structure (WSS) and the Amman-Hallabat Structure (AHS) (Figure 1a,b). The DSTF is one of the longest active sinistral strike-slip fault systems (~1100 km length) in the world [13,14]. The terms WSS [15] and AHS [16] were introduced to describe the transpressional deformation pattern within the region (Figure 1a,b). They consist of two sinistral NE-SW-trending strike-slip faults, which are the Wadi Shueib Fault (WSF) and the Amman-Hallabat Fault (AHF) (Figure 1b), and NNE-SSW- to NW-SE-trending fold systems [17–19]. To the best of the authors' knowledge, the deformation pattern of the WSF and AHF has not been studied previously at this large scale. The WSF and AHF are located east of the previously mapped regional active tectonic Wadi Arab Fault (WAF) zone, which is part of the DSTF in Jordan (Figure 1a,b). However, very little research has been performed to trace the true extent of fault segments such as these on land. The role of these faults in shaping the architecture of the highly deformed study area has thus remained largely unknown. Thus, in this research we tried to address this problem to some extent by mapping the small- and large-scale fault segments on the surface. Structurally, the presence of faulting in any area is based on the displacement of rock layers (e.g., [12]). However, most of the faults are buried underneath recent deposits and appear as surface geological features expressed as lineaments. Lineaments are interpreted as surface expressions of geologic weak zones as well as faults and rock fractures that are most likely related to the regional tectonic activity and geodynamic setting, which can be properly detected only through remotely sensed data (e.g., [12,20–26]). Lineament mapping plays an essential role in elucidating the tectonic behavior of a tectonically active area [27]. Moreover, the dominant lineament directions can provide information about the regional fracture pattern and its relationship to the major tectonic elements therein [28–31].

Remote sensing data can be obtained in multi-sensor, multi-resolution, multi-frequency, and multi-temporal forms that enable the integration of data from various sources and various typologies. The use of multi-sensor image data is increasingly becoming an important component of digital image processing because it increases the user's ability to simultaneously analyze complementary information [32,33]. Satellite images and aerial photographs are extensively used to extract lineaments for different purposes at various scales [34].

Remote sensing analysis is carried out using image processing software, such as PCI Geomatica, ArcGIS 10.7, and ENVI 5.3. The motivation of our research was to elucidate the geological structures of the study area by mapping the lineaments using optical remote-sensed satellite images. The integrated remote sensing and geographic information system (GIS) techniques can provide a relatively fast and inexpensive way of detecting and locating hidden geological structures. The use of remote sensing techniques in this research was mainly directed towards detecting the direct effects where the geological features (i.e., Lineaments) themselves can be investigated and extracted or proxy effects where a localized near-surface feature can cause a localized change in a surface property (land cover). This approach allowed the detection of variations in the topsoil properties if they were adequately measured using multispectral remote sensing imaging, which can yield potential information about the exact spatial locations and extensions of buried geological structures.

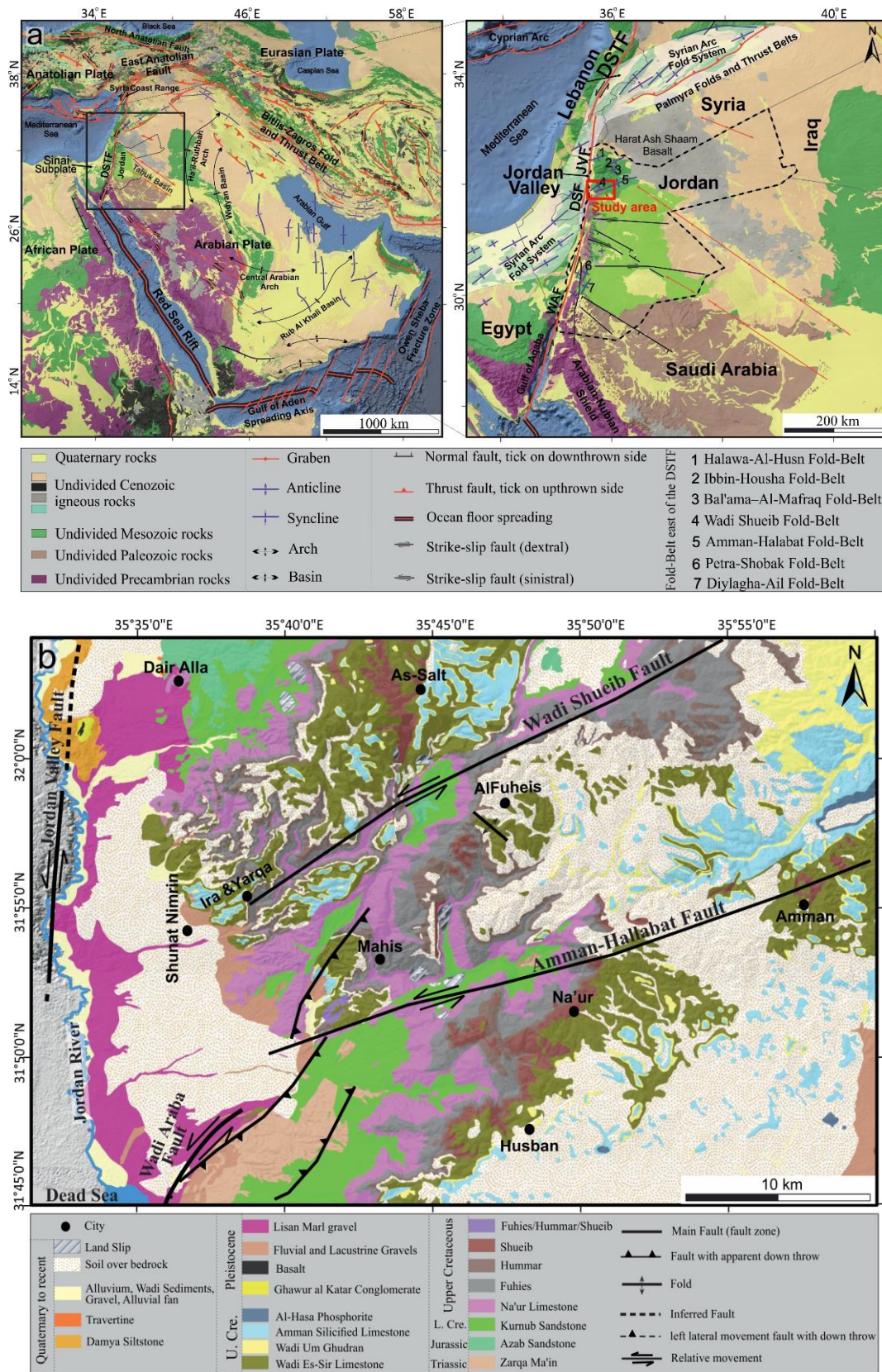


Figure 1. (a) A generalized map of geological units (based on [35,36]) and the main tectonic elements of the Middle East region compiled from [37–46]. The location of the fold-belts east of the Dead Sea Transform is based on Atallah [47,48], and that west of it is based on Chaimov et al. [49]. DSF: Dead Sea Fault; JVF: Jordan Valley Fault; WAF: Wadi Araba Fault. (b) Detailed geological map of the study area (modified from [50–53]).

In our research, a Landsat-8 OLI image was used for automated lineament feature extraction. Lineament mapping was facilitated by reprocessing and digital image enhancement using the principal component analysis (PCA) of existing Landsat image datasets. Additional information also was obtained from the field observation of the study area for a greater structural correlation. This research aimed to build a better structural framework of the WSS and AHS with respect to the regional tectonic pattern of the DSTF and provide new findings using remote sensing that support previously published studies based on field observation.

2. Previous Studies

The name “Wadi Shueib Structure” (WSS) was introduced by Mikbel and Zacher [15] to describe the fold-belt that begins from the Jordan Valley and extends to the south of the Zarqa city (Figure 1a,b). It was initially called the “As-Salt Monocline Flexure” by Burdon [54], who contended that a thrust fault in the basement rocks produced by SE compression stress gave rise to the formation of a monocline structure. That same structure also was referred to as “the Suweileh Structure” by Bender [55].

The AHS was first defined as a monocline and narrow fold-belt by Quennell [56]. Mikbel and Zacher [16] described the structure as a fold-belt that starts from the NE corner of the Dead Sea and extends in the NE direction as a system of tight anticlines and synclines. The fold-belts east of the DSTF were previously described as either normal faults or flexures (Figure 1a). More extensive studies thereafter defined these structures as a zone of folding caused by the accumulation of the NW-SE compressional stresses on the Arabian plate since the Late Cretaceous time [15,16,47,57,58]. Different studies have pointed out that some of these folds were most-likely formed as part of the Syrian Arc Fold System [47,57,59]. Newer studies have documented more recent fault movements in different places along with both structures, and the authors were able to relate these movements to the active major stress field of the DSTF from the mid-Miocene time to the present day (e.g., [18,19,60]).

A plethora of studies have been carried out to enhance geological knowledge and to revise existing geological maps by using optical remotely sensed data, finding new faults that were previously unmapped (e.g., [61–67]). For example, Langridge et al. [61] assessed the potential for generating sub-5 m bare earth digital elevation models (DEMs) from ground return data in areas of varying degrees of dense rainforest cover and relief as an aid to mapping portions of the Alpine and Hope faults in New Zealand. They derived the DEMs from airborne light detection and ranging (LiDAR), and their derived high-quality and high-spatial-resolution DEMs from the LiDAR data supported them in recognizing and mapping the details of many fault-displaced landforms and other geomorphic features that were previously unknown. The results of Langridge et al.’s study show the great potential and limitations of LiDAR as a cost-effective, useful tool for the precise mapping and examination of active faults and other geomorphic features that are covered by dense growth forests worldwide. Radaideh et al. [62] investigated the dominant orientations of morphological features and the relationship between these trends and the spatial orientation of tectonic structures in SW Jordan. They used Landsat-8 and hill-shaded images, which were derived from 30 m-spatial-resolution Advanced Spaceborne Thermal Emission and Reflection Radiometer (ASTER-DEM) data. In their study, they applied remote sensing and GIS techniques, using both datasets for the automatic extraction of morphological features, mapping geological lineaments, and determining drainage patterns. To overcome the limitations of the lighting’s effect on the appearance of linear features, the multi-oblique-weighted (MDOW) shaded relief method [63] was used by the authors to generate a hill-shaded image illuminated with different azimuth angles of the light source. Depending on the illumination azimuth and tilt selection, the features are either obscured or highlighted in a hill-shaded image. The features parallel to the light beam were not identified as easily as those oriented perpendicularly to the illumination. In addition, some of the linear features identified at one azimuth angle of the light source were not apparent or were poorly visible at another angle.

3. Regional Tectonic Setting

The DSTF is an N-S-trending continental plate boundary that transforms the crustal structure that separates the Arabian plate on the east from the Sinai sub-plate on the west, connecting the divergent plate boundary in the Red Sea with the convergent plate boundary in the East Anatolian Fault (Taurus-Zagros compressional front) (Figure 1a: [67–72]). Tectonically, the DSTF can be subdivided into three fault segments (Figure 1a: e.g., [73,74]): (i) the southern segment extending from the Gulf of Aqaba (Red Sea) through the Jordan Valley; (ii) the central NE-SW-trending segment running through Lebanon and SW Syria; and (iii) the N-S-trending segment adjacent to the Syrian Coast Range. In the Jordan region, the DSTF consists of three fault segments (Figure 1a): (1) the Wadi Araba Fault (WAF) to the south, (2) the Dead Sea Fault (DSF) in the middle, and (3) the Jordan Valley Fault (JVF) to the north [72]. The onset of the formation of the DSTF has been dated to around 14 Ma (i.e., Middle Miocene) [75]. The regional tectonics of the continental part of the Arabian plate (including Jordan) have been studied previously through macrostructures (e.g., [15,16,47,54,55,76–78]). Other authors have studied the regional tectonics with a special focus on mesostructures (e.g., [17,44,53,60,79–85]). Regional plate motion studies have used the fault orientation, additional local observations, and constraints from the motion of adjacent plates to estimate a 5–10 mm/y relative motion across the DSTF (e.g., [14,86,87]). Local geological and seismic studies that estimate the slip-rate across the DSTF yield a wider range of relative motion estimates, from 1 to 10 mm/y (e.g., [88–95]). The estimated slip-rate is based on the accumulated offset of 107 km of the pre-Miocene rocks east and west of the transform. Using aerial photograph analysis and earthquake catalog information of the DSTF, Garfunkel et al. [72] concluded that the present-day slip-rate has been slower (1.5–3.5 mm/y) than the Pleistocene rates (2.58–0.0117 mm/y). Recent studies on offset alluvial fan surfaces and drainage systems along the northern WAF have suggested slip-rates of 4 mm/y [96] and 4.7 mm/y [97]. Hence, the relative plate movements along the DSTF are responsible for most of the active deformation between the Arabian and African-Sinai plates (e.g., [97]). Based on high-resolution GPS measurements, Alchalabi et al. [74] proposed that part of the deformation of the northern DSTF could be accommodated by other structures, such as the fault and fold zones. Diabat et al. [17] categorized the stress field east of the DSTF into two compressional stress systems: (1) the NNW-SSE-trending Dead Sea System (DSS) and (2) the NW-SE-trending Syrian Arc System (SAS) (Figure 1a). According to Quennell [14] and Zain Eldeen et al. [83], from the Late Cretaceous time to present day, Jordan has been affected by three main compressional stress systems: the ENE-WSW-, NW-SE-, and NNW-SSE-trending stresses.

4. Geological Setting of the Study Area

The following stratigraphic description of the study area is based on previous studies by Burdon [54], Bender [98], Powell [99], and Powell and Moh'd [100]. Additional information was also obtained from field observations for a better lithological correlation (Figure 2). The major geological units in the study area range in age from the Jurassic to the Upper Cretaceous periods. The Jurassic outcrops are composed mainly of yellowish dolomite, limestone, and marly limestone [101]. They are outcroppings in the eastern part of the study area as an isolated exposure, in the core of an anticline, 1 km to the southwest of Mahis village (Figure 1b).

Three megasequences are recognized within the Cretaceous to Eocene sedimentary succession: (1) the Kurnub Group, (2) the Ajlun Group, and (3) the Belqa Group (Figure 2, [54,99,100]). The Lower Cretaceous rocks are represented by the Kurnub Group, which is predominantly comprised of a thick deposit of massive white to reddish, medium to coarse-grained sandstone, which was deposited in alluvial environments with an upward trend from a braided system then a low and then high sinuosity alluvial plain [98,100]. The Kurnub Sandstone overlying the Jurassic rocks crops out in different places of the study area (Figure 1b). The Upper Cretaceous Ajlun and Belqa Groups reflect a shallow-marine environment and are represented by carbonates, chert, and phosphate [99]. The Ajlun Group is subdivided into five main formations (Na'ur, Fuhies, Hummar, Shueib, and Wadi Es-Sir) (Figure 2). The Na'ur, Fuhies, and Hummar Formations are of Cenomanian age [99]. The Shueib Formation

(Late Cenomanian–Early Turonian) consists mainly of nodular limestone, marl, marly limestone, dolomitic limestone, coquina, fossiliferous limestone, and nodular marly limestone (Figure 2). It is overlain by the prominent cliff-forming Wadi Es-Sir Formation of Turonian age [99].

In our study area, the overlying Belqa Group consists of chalk, chert, and phosphorite deposited in a pelagic or hemipelagic ramp setting [100]. It is subdivided into five main formations that are the Um Ghudran, Amman, Al-Hasa, Muwaqqar, and Um Rijam [99]. The Um Ghudran Formation was deposited in a moderate to deep-water pelagic environment, belongs to the Coniacian–Santonian age, and represents the basal part of the Belqa Group [99]. It is up to 15 m thick and consists of massive, white buff–grey, hard, detrital chalk that contains fish teeth, shell fragments, and thin layers of chert (Figure 2). The overlying Amman Formation consists mainly of silicified limestone and belongs to the Santonian–Campanian age [99]. The Al-Hasa Formation consists of thin to medium-bedded phosphate, cherty phosphate, limestone, coquina, and marl. The Amman and Al-Hasa Formations were deposited in a shallow-marine environment [99]. The Pleistocene rocks are represented by the Jordan Valley Group and consist mainly of conglomerate, sandstone, claystone, and basalt flow [98]. In the study area, this group is subdivided into three main formations: the Ghawur al Katar, Lisan, and Damia (Figure 1b). The Ghawur al Katar Formation was deposited in a deep-water environment, the Lisan Formation was deposited in a shallow-water pelagic environment, and the Damia Formation was deposited in a wet continental environment. A basalt flow is only exposed in one location to the southwest of Dair Alla city (Figure 1b). It is an NNE-SSW-trending feature that follows the direction of the DSTF [102].

Quaternary deposits of recent sediments cover almost the entire western part of the study area (Figure 1b) and are mainly composed of unconsolidated materials, such as gravel, sand, and silt, which were produced by sediments dumped along wadies during periods of floods [98].

Era	Period	Epoch	Age (Ma)	Group	Formation		
Cenozoic	Quaternary	Holocene to recent	0.01	Jordan Valley	Alluvial fans, wadi and lake sediments		
		Pleistocene	2.60		Lisan		
	Neogene	Pliocene	5.30		Undifferentiated		
		Miocene	23.0				
	Paleogene		Oligocene	33.9	Belqa	Umm Rijam Chert	
			Eocene	56.0		Muwaqqar Chalk Marl	
			Paleocene	66.0		Al-Hasa Phosphorite	
	Mesozoic	Cretaceous	Maastrichtian	72.1		Belqa	Amman Silicified
			Campanian	83.6			Wadi Umm Ghudran
			Santonian	86.3			Ajlun
Coniacian			89.8	Shueib			
Turonian			93.9	Hummar			
Upper			Cenomanian			Fuhies	
						Na'ur	
Lower			Albian	100	Kurnub Sandstones		
			Aptian	113			
			Neocomian	126			
				145			
Jurassic	Lower and Middle		201			Azab Sandstone Group	
Triassic	Lower		250	Ramtha	Zarqa-Ma'in		

Figure 2. A geologic columnar section of the study area showing the dominant lithologies, groups, and formations and the ages (modified from [50–55,98–100]).

5. Materials and Methods

There are several features that are indicative of faulting in the field, which include the following: the offset of the marker horizons; the juxtaposition of rock units that were not in contact when first formed; the omission or repetition of sections; and the presence of slickensides surfaces, slip lineations, fault breccias, and fault-related folds. Displacement along major strike-slip faults, such as the AHF and faults related to WSS, is not necessarily exactly parallel to the fault surface, in part due to the existence of restraining and releasing bends along the fault.

The extraction and analysis of lineaments from digitally enhanced satellite images provides basic sources of information for regional structural and tectonic studies. The geological structure analyses of this study were based on optical remote sensing satellite data from the Landsat-8 OLI Operational Land Imager. Landsat-8 OLI collects 11 spectral bands with a spatial resolution of 30 m for Bands 1–7 and 9, 15 m for the panchromatic band (Band 8), and 100 m for the thermal bands (Bands 10 and 11).

The study area was covered by one scene of Landsat-8 OLI (Path 174 and Row 38), which is freely available from the United States Geological Survey (USGS) Global Visualization Viewer (GLOVIS) portal and was acquired on June 10, 2019. To extract the lineament features from the Landsat-8 OLI scene, several processing steps were required as shown in Figure 3.

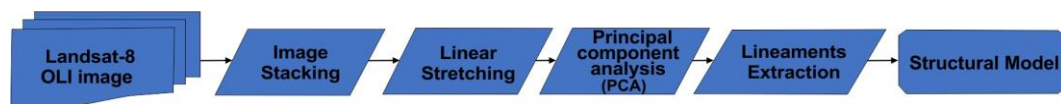


Figure 3. Flowchart methodology of the study.

The utilized image coordinate was projected to the Universal Transfer Mercator (UTM) coordinate system. Then, the composite bands of all of the multispectral bands were combined into a single file to create a full image and were pan-sharpened to a 15 m spatial resolution to match the panchromatic band. To analyze the remotely sensed images, the different images representing the different bands were stacked using the ArcGIS 10.7 software [103], which allowed for different combinations of colors to be shown, including natural (true) and false color composite representations. A true-color composite is one in which the colors have been assigned to digital number (DN) values that represent the visual spectral range of the colors used in the image [104]. Bands 4 (red band), 3 (green band), and 2 (blue band) of an OLI image were assigned respectively to the R, G, and B colors for displaying a “true-color” image in this study. The output image of a true-color composite is shown in Figure 4.

Thereafter, the full scene was clipped to fit the boundary of the study area. Then, different band filtering and stretching techniques derived from the Landsat-8 OLI image were used to automatically extract the geologically related linear features and other discontinuities of the study area. In practice, this work was restricted to the linear stretching image enhancement processes, which were applied to the image data to display the data more effectively for subsequent visual interpretation.

Finally, PCA was used to obtain an enhanced image where the structural features and geologic lineaments were more evident, which thus eased the lineament extraction procedures that followed. PCA is a statistical technique designed to reduce redundancy in multi-spectral data, which consists of identifying the spectral differences between materials that may be more apparent in PCA images than in the individual bands [32]. PCA transforms a multivariate data set of intercorrelated variables into a dataset of new uncorrelated linear combinations of the original variables while focusing the variation of the many bands into a smaller-dimensional image dataset, thereby making the transformed dataset more interpretable than the source data. The output image used for the extraction of lineaments is shown in Figure 5 using Landsat-8 OLI Bands 6, 5, and 2. These PCAs were assigned to display colors (Red, Green, and Blue, respectively) to form a PC-color composite image.

The line-module technique within the PCI Geomatica 2018 [105] software was used to extract the lineament map for the study area. The extraction process was controlled by six different parameters: the band selection, filter process, gradient threshold, length threshold, line fitting threshold, and angular

difference threshold. Based on those parameters, several lineament maps were generated using different threshold values. The most suitable threshold value was selected, considering the obtained lineaments as fault lines. The general properties of the faults were also taken into account to determine the threshold values, such as the length, curvature, segmentation, and separation. The input parameters of the threshold-processing step were tested to select the best lineament identification. The selected threshold parameters were $RADI$ (Filter Radius) = 10, $GTHR$ (Edge Gradient Threshold) = 50, $LTHR$ (Curve Length Threshold) = 30, $FTHR$ (Line Fitting Threshold) = 3, $ATHR$ (Angular Difference Threshold) = 30, and $DTHR$ (Linking Distance Threshold) = 20. Figure 6a shows the extracted lineament map after the manual removal of the man-made artifacts from the imagery, such as vegetation cover, roads, and built-up areas. The figure also shows the major trends of these features (Figure 6b) and the extracted lineaments' overlay on the hill-shaded model of the study area (Figure 6c).

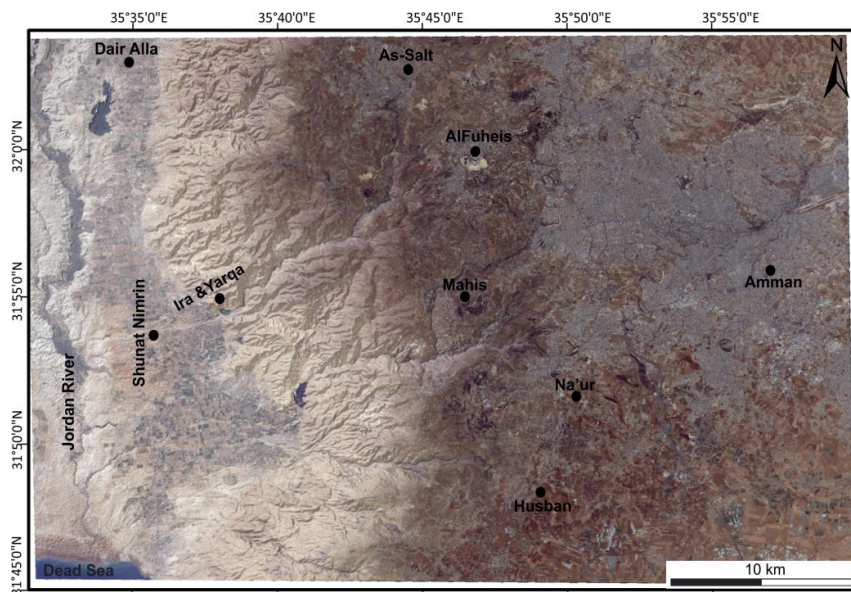


Figure 4. True-color composite (Bands 4, 3, and 2 in R, G, and B) of Landsat-8 OLI view of the study area on 10 June 2019. The image data were provided courtesy of the USGS (<http://earthexplorer.usgs.gov>).

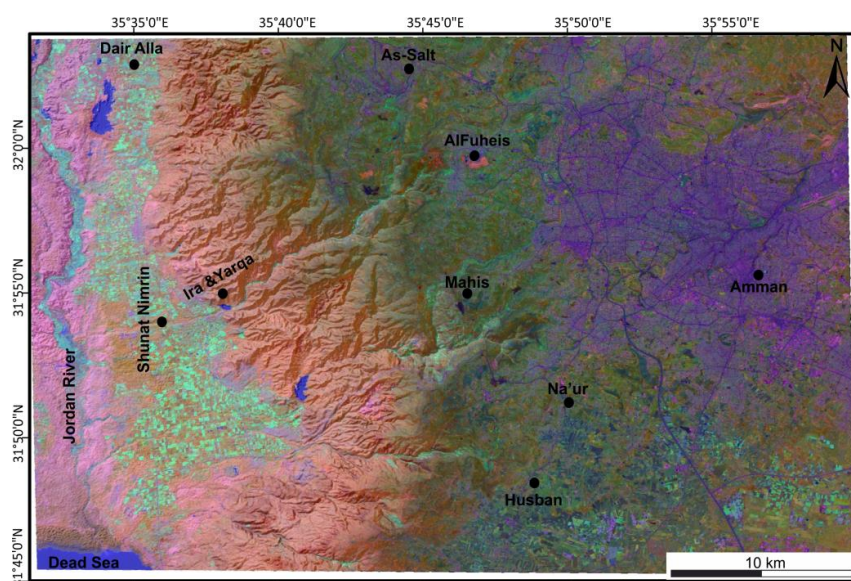


Figure 5. An example of the principal component analysis (PCA) (PC1, PC2, and PC3 in R, G, and B) developed with Landsat-8 OLI Bands 6, 5, and 2.

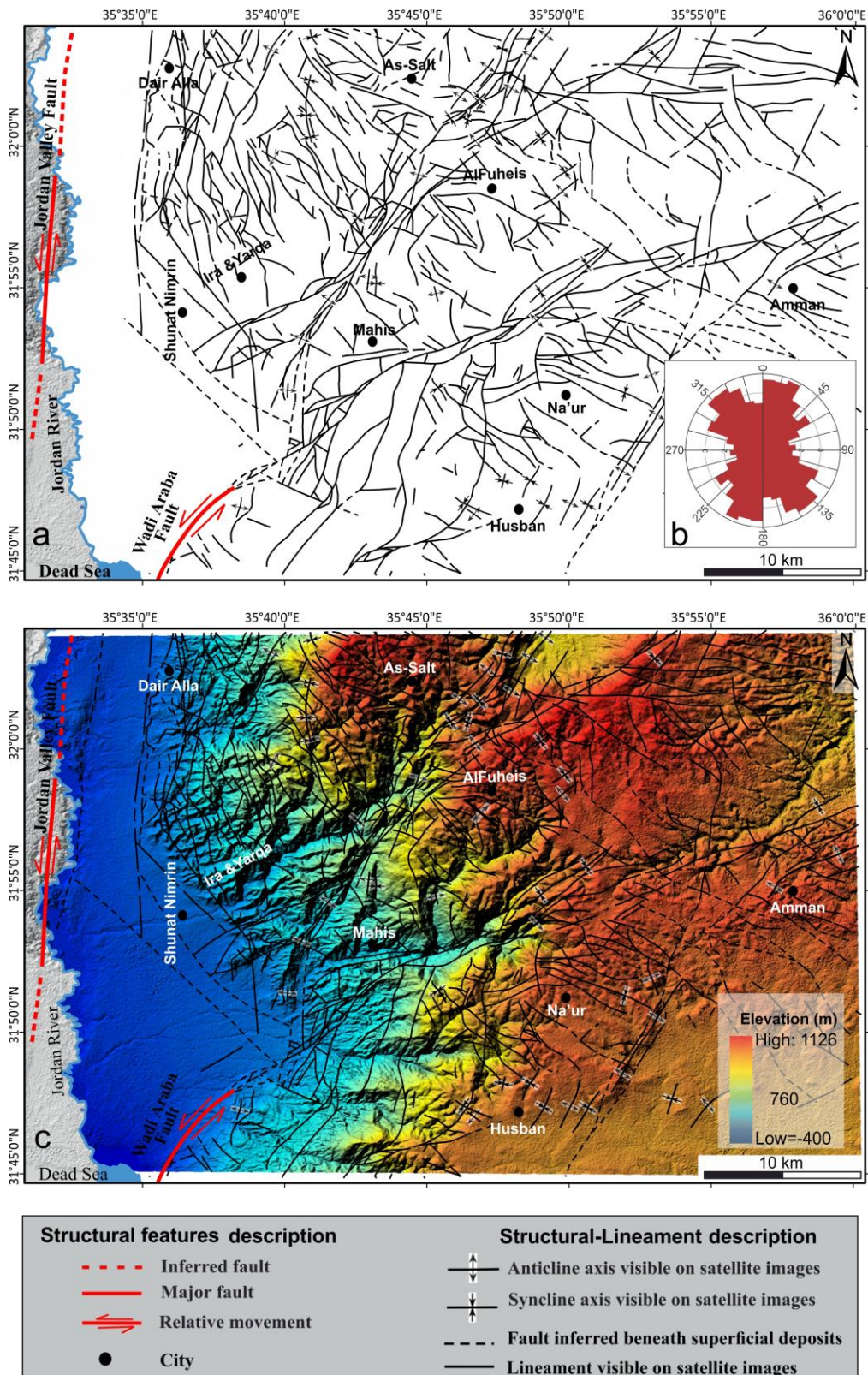


Figure 6. (a) Automated lineament map extracted from Landsat-8 OLI satellite images taken within the study area. (b) Rose diagram plot of the extracted lineaments showing two main lineament population trends based on cumulative-length weighting: NNE-SSW, NW-SE, and a minor trend NE-SW. (c) Extracted lineament overlay on the hill-shaded model of the study area (the red color represents a relatively higher elevation and the blue color represents a relatively lower elevation).

6. Results and Discussion

6.1. Lineament Density Map

The linear features shown in Figure 6a were used to produce the surface lineament distribution and lineament density map, including fault and fold systems. It is important to mention here that the extracted lineaments were uploaded on top of a Google Earth map to visually differentiate the folds from the lineament features.

Our results demonstrated a good correlation between and distribution of the structural geology from the published literature and digitalized geological map lineaments and the extracted lineaments in this study, which were validated through geological field visits (ground-truth) in the study area. It is worth noting here that the comparison between the extracted lineament map and the published fault map using GIS matching techniques showed that 60% of the lineament segments/lines in the extracted lineaments map were properly identified in the study area. The additional lineament segments we discovered that were not identified in the published literature were used to update and improve the existing structural maps of the study area.

In practice, the lineament density map was generated from the number of lineaments per unit area [106]. Figure 7 illustrates the lineament density map, which shows the concentration and spatial distribution of the lineaments within the study area. The lineament density map revealed a relatively higher concentration of lineaments in different places, over regions of high rugged topography and complex geological setting, particularly in the areas along the major fault traces. These higher-density lineament areas were observed as elongated pockets (i.e., along the extension of the WSF and AHF) (Figure 7). The lineament density map also shows a relatively lower concentration of lineaments in different places of the study area (e.g., in the southwest and between the WSS and AHS). The lower concentration of lineaments in these areas could be due to the higher thickness and/or softness of the Quaternary cover (Figure 1b) and their recent age, assuming that the development of lineaments does require some time.

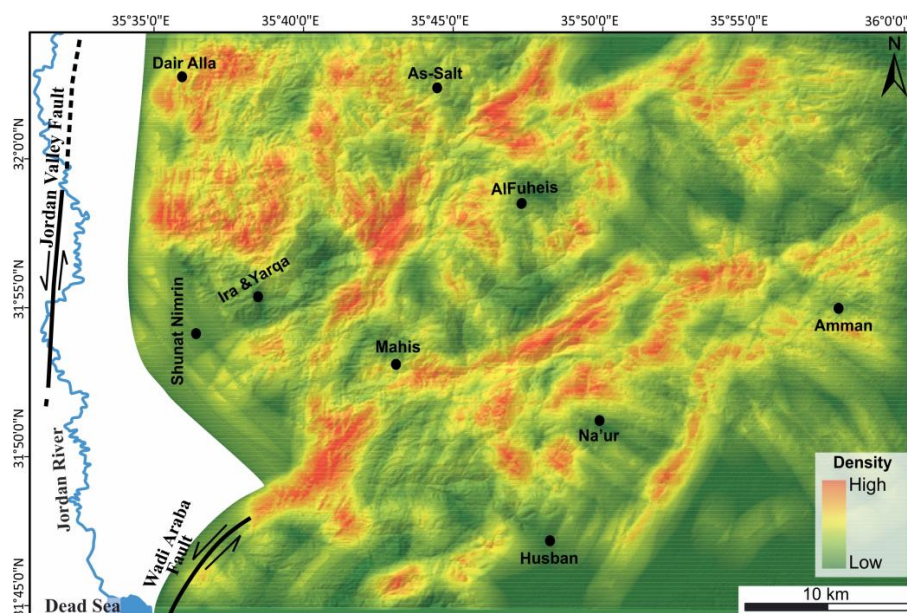


Figure 7. Lineament density map. The red color represents areas with a relatively higher density and the green color represents areas with a relatively lower density.

A rose diagram was used in this study to examine the distribution of the extracted lineaments based on the contribution of their frequency to the orientation trend. The rose diagram was created with the RockWorks.v.17 software [107] by counting each line as an element regardless of its length

(Figure 6b). Lineaments are related to large subsurface fractures and faults, where their orientation and number give an idea of the regional fracture pattern of an area [28,67]. In addition to this view of individual lineament orientations at a given point, it is possible to combine the various orientations in all directions into a single rose diagram with angles ranging from 1° to 180° as suggested by Chopra [108]. The rose diagram plot in Figure 6b shows the dominant directions for the extracted lineament population based on cumulative-length weighting. It also reveals the two main lineament population trends in the study (NNE-SSW and NW-SE) and a minor trend of NE-SW.

6.2. Tectonic Implications

Lineament mapping plays an essential role in the elucidation of the tectonic behavior of a tectonically active area [20,109,110]. Moreover, the dominant lineament direction of an area can give an idea about the regional fracture pattern and relationship between the major tectonic elements and the geodynamic setting [110]. In the study area, the formation of the WSS and AHS was attributed to the NW-SE-trending Syrian Arc compressional stress field during the Late Cretaceous period [47,56,58]. They were redefined as active structures since the Quaternary time [19,59,111], and as transferring part of the tectonic stress through the WAF [19,111]. According to the authors of the above publications, the WSS and AHS have been reactivated in response to two different mechanisms: 1) the AHS directly receives a small part of the tectonic stress through the WAF, while 2) the WSS acts as a sinistral transfer fault of a transtensional zone composed of numerous NE-SW normal faults active in the Quaternary period.

The most recent study on the WSS and AHS was conducted by Al-Awabdeh et al. [19], who based their interpretations on fieldwork measurements; the authors introduced a schematic sketch of the tectonic evolution of both structures from the Late Cretaceous to Pliocene period (Figure 8a,b). Their suggested sketch shows the present-day configuration of the WSS and the AHS due to the Miocene reactivation by the stress field of the DSTF and the proposed northern closure of the Dead Sea Basin. The identified lineament map in this study (Figures 6a and 9) shows new fault systems and several significant fold structures that were not mapped previously by the fieldwork documented in Al-Awabdeh et al. [19].

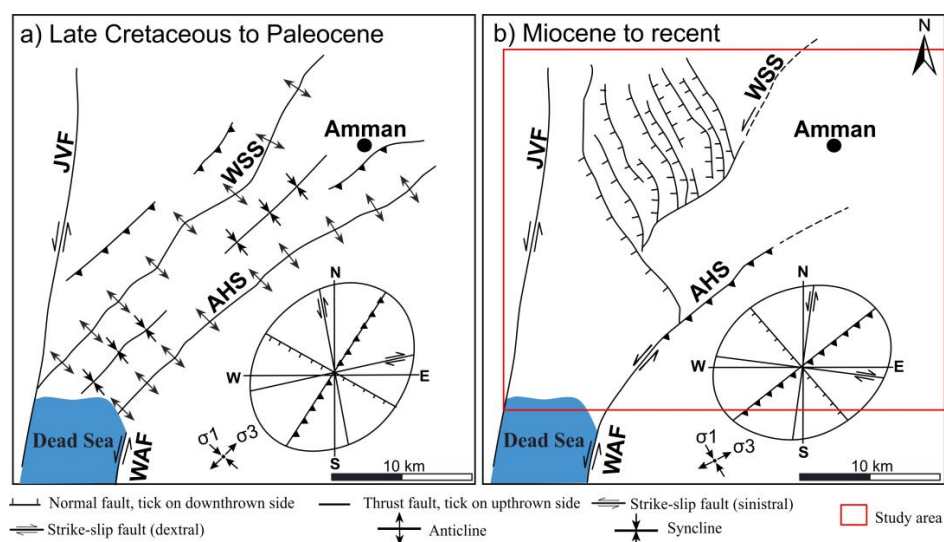


Figure 8. Schematic sketch of the tectonic evolution of the WSS and the AHS modified from Al-Awabdeh et al. [19] (a) from the Late Cretaceous to Paleocene period; and (b) the present-day configuration of the WSS and the AHS due to the Miocene reactivation by the transpressional stress field of the Dead Sea Transform Fault (DSTF). The stress field orientation is based on [17,60,83,112]. AHS: Amman-Hallabat Structure; JVF: Jordan Valley Fault; WAF: Wadi Araba Fault; and WSS: Wadi Shueib Structure.

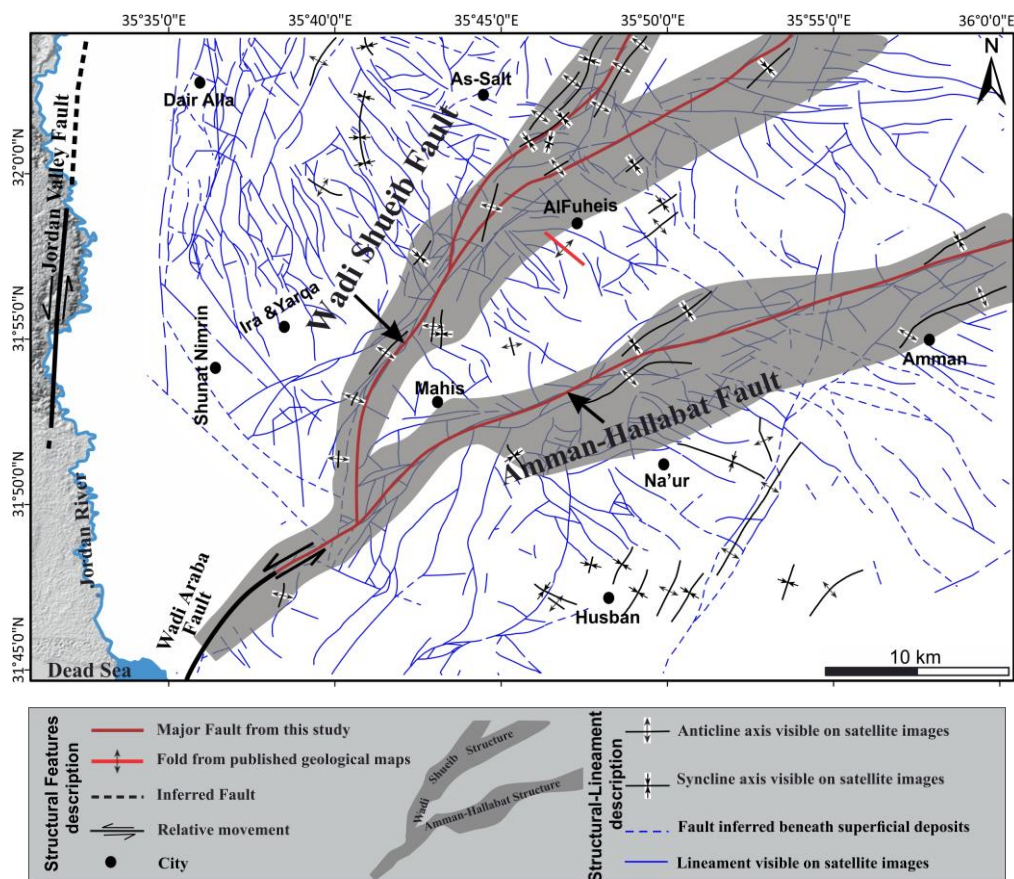


Figure 9. Configuration of the Wadi Shueib and Amman-Hallabat Faults and their spatial relationship with the Wadi Araba Fault.

It is worth noting here that the comparison between the extracted lineament map of this study (Figure 9) and the published fault map of Al-Awabdeh et al. [19] (Figure 8b) shows an update of the location (and in some places the trajectory) of the WSF and AHF. Thus, the identified lineament map provides new findings that modify the existing published data.

The termination of the strike-slip WAF, as a segment of the DSTF, represents a puzzle for geologists studying the evolutionary history of the transform and its related structures to the east. However, the extension of the WSF and AHF from the lineament map (Figure 9) shows that the southwestern extension of the WSF merges with the southwestern extension of the AHF. Furthermore, the WAF joins the faults of the WSS and AHS at the northeast corner of the Dead Sea. These observations are in good agreement with the interpretations of Al-Awabdeh et al. [19].

Our reconstruction of the structural deformational style of the WSF and AHF and their spatial relationship with the WAF is consistent with the assumption that these faults may have developed as splay or horsetail faults at the endpoint of the WAF (Figure 10a). It is well-known, in structural geology, that extensional horsetail splays may host sedimentary basins while compressional horsetail splays may display thrust faults and folds at the tips of major strike-slip faults (e.g., [12]). Based on this accepted supposition, we further suggest that the WSF and AHF were reactivated as restraining bends composed of active strike-slip fault branches and folds that developed due to the NNW-SSE-trending Dead Sea transpressional stress field (Figure 10b,c). This interpretation refers to the kinematically induced stress field mechanism that is locally induced by the relative movement along the DSTF of the Arabian plate and Sinai Subplate. Such a mechanism is plausible way of explaining the multi-scale relationship between deformation and stress in the various geodynamic settings. For a general description of the mechanism, see, for example, [113]. At each scale, the deformations produced

by the outer stresses induce inner stress regimes within the influence area, which, in turn, produce smaller scale deformations [113,114]. In the study area, the regional scale plate movement produces, in the influence area of the DSTF, a local stress regime responsible for the observed transpressional deformation along the WSF and AHF as a result of the shear transmitted through the WAF.

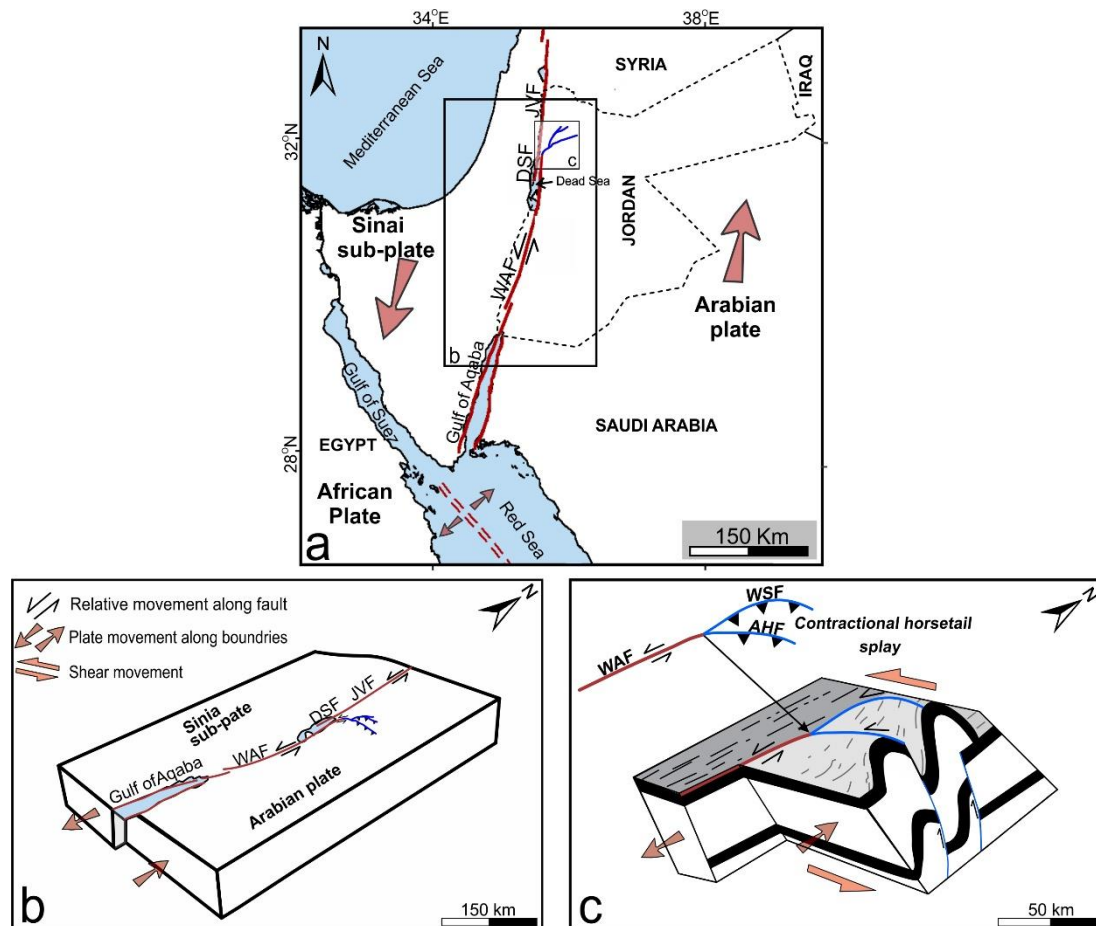


Figure 10. (a) Tectonic map of the eastern Mediterranean, showing the plate boundaries and major segments of the DSTF along the Jordan (compiled from [37,38,41,45]). (b) The simplified sketch shows how the Wadi Shueib and Amman-Hallabat Faults splay as horsetail structures from the WAF. (c) The conceptual model illustrates the transpressional Wadi Shueib and Amman-Hallabat Faults along with the northern termination of the WAF (the model has no vertical exaggeration). The model suggests that both structures are reactivated splays within the area of the restraining bend. Fault splays comprising contractional horsetail structures. Depending on the direction of curvature to the sense of displacement, thrust components of displacement occur on faults of the horsetail, and these movements are accompanied by folding and uplifting. AHF: Amman-Hallabat Fault; DSF: Dead Sea Fault; JVF: Jordan Valley Fault; WAF: Wadi Araba Fault; WSF: Wadi Shueib Fault.

Depending on the relationship between the direction of the WSF and AHF strands and the regional tectonic displacement along the WAF, a thrust component occurs on the faults with horsetail geometry. These movements are accompanied by folding and uplifting (Figure 10c); therefore, the WSF and AHF represent contractional horsetail structures with associated folding and thrusting deformation. Our observations are consistent with the conceptual models of Cunningham et al. [115] for tectonic features associated with strike-slip restraining bends. Our interpretation in this study contributes to our geological knowledge base and improves the existing geological maps of the area. Although transtensional horsetail structures have been previously described at different segments of

the DSTF [102], the transpressional horsetails have been described only at the end of the strike-slip fault bordering the eastern margin of the Gulf of Aqaba [116,117].

According to Bowman et al. [118], strain partitioning is a characteristic of oblique-slip and can be explained by the upward elastoplastic propagation of a localized basement fault or a shear zone at depth. They illustrated that the static stress field above a pure strike-slip fault at depth is a simple strike-slip stress field, while a buried oblique-slip fault tip propagating from depth separates into an arrangement of discrete zones of different styles of deformation, such as normal, reverse and strike-slip faulting.

Generally, the partitioning of transpressional strain occurs when stress is applied obliquely to pre-existing structural weaknesses, or during later stages of progressive strain when the early deformation of isotropic rocks imparts sufficient anisotropy to allow the subsequent strain to be partitioned [12,119,120]. In the case of the WSF and AHF, we propose that strain partitioning occurred when the NNW-SSE-trending Dead Sea transpressional stress field was applied obliquely to pre-existing structural weaknesses of these fault systems. Paleostress analysis, particularly along with the WSS and AHS, showed that σ_1 and σ_3 of the recent stress field are almost horizontal and NNW-SSE- and ENE-WSW-striking, respectively, and σ_2 is vertical [17,60,80–83,112].

According to Diabat [60], the Amman-Hallabat strike-slip fault changed direction along its strike in many places outside the study area, particularly east of Amman, accompanied by a vertical component, resulting in either transpression or transtension. Extensional structures, such as the NW-trending normal faults, and compressional structures, such as NE-trending folds and reverse faults, are believed to have resulted in the association of the major strike-slip system with σ_1 swinging around the N-NW direction as deduced from the paleostress results. This event produced three different stress states related to the major fault (AHF): (1) sub-horizontal (σ_1), oblique to the strike of the adjacent fault segment, with sub-vertical (σ_2), and sub-horizontal (σ_3); (2) sub-horizontal (σ_1), perpendicular to the strike of the major fault, with sub-vertical (σ_2), and sub-horizontal (σ_3), subparallel to the strike of the major fault; and (3) sub-vertical (σ_1), with NE-oriented (σ_3) parallel to the major AHF and perpendicular to the NW-trending faults and sub-vertical (σ_2). Variation in the directions of the principal stresses may either reflect the later reactivation of the AHF due to stress changes over time or stress changes due to the position along the major fault.

This situation can be explained as a switch of the stress axes σ_1 and σ_2 that occurs during active tectonic events and partitioned strike-slip deformation. In the study area, we found this activity to be consistent with the present-day stress field and to be responsible for the active NW-SE normal faults and the reactivation of pre-existing structures as the WSS and AHS [17,60,111]. Furthermore, the role of the transform fault, such as the DSTF, is to accommodate the relative motion between adjacent blocks, and depending on the changing geometry of the fault and/or changes in the relative movements, it can generate switches and partitions as indicated in our study. These observations are in very good agreement with the suggested model of this study that explains the structural deformational style of the strike-slip regime along the WSF and AHF and their related structures.

7. Conclusions

This paper presented the results of the study we conducted to understand the structural deformation style of the strike-slip regime along the WSS and AHS in NW Jordan using a combination of remote sensing analysis and GIS techniques. This region is highly faulted and has a complex geological pattern. It contains prominent geological features and is bounded to the east by a portion of the DSTF. Our lineament analysis revealed an effective tool for mapping out the exact location/elongation of the major faults of these structures (WSS and AHS) and modifying existing structural maps of the study area as well.

We analysed images of the study area from PCA for automatic lineament extraction under the user-suggested parameter values from several setting tests within the LINE module of the PCI Geomatica software. The extracted lineament density map revealed a higher concentration of

lineaments in different parts of the study area, particularly over regions of high rugged topography and complex geological settings. These higher-density lineament areas were observed as elongated pockets along the extension of the WSF and AHF. The lineament density map also revealed a relatively lower concentration of lineaments in different places of the study area (i.e., in the southwestern area and between the WSS and AHS). The lower concentrations of lineaments in these places could be due to the higher thickness and/or softness of the Quaternary cover and their recent age, assuming that the development of lineaments does require some time.

Our results show a good correlation between and distribution of the lineaments we extracted and the structural geology from the previously published literature and the digitalized lineaments from the geological maps, which we validated through geological field visits (ground-truth) in the study area. Furthermore, our comparison, using GIS-matching techniques, between the extracted lineament map and the published structural maps revealed that 60% of the lineament segments/lines in the extracted lineament map were properly identified in the study area. The additional lineament segments that were not identified in the literature were used to update and improve the existing structural map of the study area.

Based on our lineament map, the southwest extension of the WSF merges with the southwest extension of the AHF, and the WAF joins both faults in the northeast corner of the Dead Sea. The observed structural style of the WSF and AHF and their spatial relationship with the WAF are in good agreement with the assumption that these faults developed as splay or horsetail faults at the endpoint of the WAF. It is a plausible assumption that the WSF and AHF were reactivated as restraining bends composed of active strike-slip fault branches that developed due to the NNW-SSE-trending Dead Sea transpressional stress field. This interpretation refers to the kinematically induced stress field mechanism, which was locally induced by the relative movement between adjacent blocks along the DSTF of the Arabian plate and Sinai Subplate. This mechanism is a valuable way of explaining the multi-scale relationship between deformation and stress in various geodynamic settings. At each scale, the deformations produced by outer stresses induce inner stress regimes within the influence area, which, in turn, produce smaller-scale deformations. In the study area, the regional scale plate movement produced, in the influence area of the DSTF, a local stress regime responsible for the observed transpressional deformation along the WSF and AHF as a result of the shear transmitted through the WAF.

Depending on the relationship between the directions of the WSF and AHF strands and the regional tectonic displacement along the WAF, thrust components may occur on faults with horsetail geometry, and these movements are accompanied by folding and uplifting. Thus, the WSF and AHF represent contractional horsetail structures with associated folding and thrusting deformation. Our research observations are consistent with the conceptual models for the tectonic features associated with strike-slip restraining bends.

Author Contributions: Conceptualization, M.A.H. and A.A.-R.; methodology, M.A.H., and A.A.-R.; software, A.A.-R., M.A.H., and M.A.-Z.; validation, M.A.H., A.D., G.J., and M.A.-T.; formal analysis, M.A.H., A.A.-R., and M.A.-Z.; investigation, M.A.H., A.A.-R., and A.D.; resources, A.A.-R., M.A.H., and M.A.-Z.; data curation, A.A.-R., M.A.H., and M.A.-Z.; writing—original draft preparation, M.A.H. and A.A.-R.; writing—review and editing, A.A.-R., G.J., H.G., A.D., M.A.-T., and M.A.; visualization, M.A.H., A.A.-R., and H.G. All authors have read and agreed to the published version of the manuscript.

Funding: This research received no funding.

Acknowledgments: The authors appreciate the support of the Department of Geology at The University of Jordan for this research. We also are grateful to Mahmoud Almousa for his technical support and to Elise Al-Rawabdeh for providing language editing during the course of this research. Insightful comments by Paola Cianfarra and anonymous reviewers helped to greatly improve this work.

Conflicts of Interest: The authors declare they have no conflicts of interest.

References

1. Moody, J.; Hill, M. Wrench-fault tectonics. *Geol. Soc. Am. Bull.* **1956**, *67*, 1207. [[CrossRef](#)]
2. Wilcox, R.E.; Harding, T.P.; Seely, D. Basic wrench tectonics. *AAPG* **1973**, *57*, 74–96.

3. Sanderson, D.; Marchini, W. Transpression. *J. Struct. Geol.* **1984**, *6*, 449–458. [[CrossRef](#)]
4. Bond, G.; Christie-Blick, N.; Kominz, M.; Devlin, W. An early Cambrian rift to post-rift transition in the Cordillera of western North America. *Nature* **1985**, *315*, 742–746. [[CrossRef](#)]
5. Sylvester, A. Strike-slip faults. *Geol. Soc. Am. Bull.* **1988**, *100*, 1666–1703. [[CrossRef](#)]
6. Storti, F.; Holdsworth, R.; Salvini, F. *Intraplate Strike-Slip Deformation Belts*; Geological Society: London, UK; Special Publications: London, UK, 2003; Volume 210, pp. 1–14. [[CrossRef](#)]
7. Pluijm, B.; Marshak, S. *Earth structure: An Introduction to Structural Geology and Tectonics*; Norton: New York, NY, USA, 2004.
8. Kim, Y.-S.; Sanderson, D.J. Structural similarity and variety at the tips in a wide range of strike-slip faults: A review. *Terra Nova* **2006**, *18*, 330–344. [[CrossRef](#)]
9. Yu, Y.; Wang, X.; Rao, G.; Wang, R. Mesozoic reactivated transpressional structures and multi-stage tectonic deformation along the Hong-Che fault zone in the northwestern Junggar Basin, NW China. *Tectonophysics* **2016**. [[CrossRef](#)]
10. Kim, Y.-S.; Andrews, J.R.; Sanderson, D.J. Damage zones around strike-slip fault systems and strike-slip fault evolution, Crackington Haven, southwest England. *Geosci. J.* **2000**, *4*, 53–72. [[CrossRef](#)]
11. Fossen, H.; Tikoff, B. The deformation matrix for simultaneous simple shearing, pure shearing and volume change, and its application to transpression-transtension tectonics. *J. Struct. Geol.* **1993**, *15*, 413–422. [[CrossRef](#)]
12. Fossen, H. *Structural Geology*, 2nd ed.; Cambridge University Press: Cambridge, UK, 2016.
13. Quennell, A.M. *Tectonics of the Dead Sea Rift. International Geological Congress 20th*; Association of African Geological Surveys: Mexico City, Mexico, 1959; pp. 385–403.
14. Garfunkel, Z. Internal structure of the Dead Sea leaky transform (rift) in relation to plate kinematics. *Tectonophysics* **1981**, *80*, 81–108. [[CrossRef](#)]
15. Mikbel, S.; Zacher, W. Fold structures in northern Jordan. *Neues Jahrbuch für Geologie und Paläontologie. Monatshefte* **1981**, *4*, 248–256.
16. Mikbel, S.; Zacher, W. The Wadi Shueib structure in Jordan: *Neues Jahrbuch für Geologie und Paläontologie. Monatshefte* **1986**, *9*, 571–576.
17. Diabat, A.; Atallah, M.; Salih, M. Paleostress analysis of the Cretaceous rocks in the eastern margin of the Dead Sea Transform. *J. Afr. Earth Sci.* **2004**, *38*, 449–460. [[CrossRef](#)]
18. Al Hseinat, M. Structural Analysis of the Wadi Shueib Fold Belt, Jordan. Master's. Thesis, Yarmouk University, Irbid, Jordan, 2009.
19. Al-Awabdeha, M.; Pérez-Peñaab, J.V.; Azañónac, J.M.; Booth-Reaac, G.; Abed, A.; Atallah, M.; Galvea, J.P. Quaternary tectonic activity in NW Jordan: Insights for a new model of transpression-transtension in the southern Dead Sea Transform Fault. *Tectonophysics* **2016**, *693*, 465–473. [[CrossRef](#)]
20. Cianfarra, P.; Salvini, F. Lineament domain of regional strike-slip corridor: Insight from the Neogene transtensional De Geer Transform Fault in NW Spitsbergen. *Pure Appl. Geophys.* **2015**, *172*, 1185–1201. [[CrossRef](#)]
21. Oakey, G. A structural fabric defined by topographic lineaments: Correlation with Tertiary deformation of Ellesmere and Axel Heiberg Islands, Canadian Arctic. *J. Geophys. Res.* **1994**, *99*, 148–227. [[CrossRef](#)]
22. Fichler, C.; Rundhovde, E.; Olesen, O.; Saether, B.M.; Ruelatten, H.; Lundin, E.; Dore, A.G. Regional tectonic interpretation of image enhanced gravity and magnetic data covering the mid-Norwegian shelf and adjacent mainland. *Tectonophysics* **1999**, *306*, 183–197. [[CrossRef](#)]
23. Kudo, T.; Yamamoto, A.; Nohara, T.; Kinoshita, H.; Shichi, R. Variations of gravity anomaly roughness in Chugoku district, Japan: Relationship with distributions of topographic lineaments. *Earth Planets Space* **2004**, *56*, 5–8. [[CrossRef](#)]
24. Salem, A.; Furuya, S.; Aboud, E.; Elawadi, E.; Jotaki, H.; Ushijima, K. Subsurface structural mapping using gravity data of Hohi Geothermal Area, Central Kyushu, Japan. In Proceedings of the World Geothermal Congress, Antalya, Turkey, 24–29 April 2005.
25. Milbury, A.E.C.; Smrekar, S.E.; Raymond, C.A.; Schubert, G. Lithospheric structure in the east region of Mars' dichotomy boundary. *Planet. Space Sci.* **2007**, *55*, 280–288. [[CrossRef](#)]
26. Austin, J.R.; Blenkinsop, T.G. The Cloncurry Lineament: Geophysical and geological evidence for a deep crustal structure in the Eastern Succession of the Mount Isa Inlier. *Precambrian Res.* **2008**, *163*, 50–68. [[CrossRef](#)]

27. Kassou, A.; Essahlaoui, A.; Aissa, M. Extraction of Structural Lineaments from Satellite Images Landsat7 ETM+ of Tighza Mining District (Central Morocco). *Res. J. Earth Sci.* **2012**, *4*, 44–48.
28. Casas, A.M.; Cortes, A.L.; Maestro, A.; Soriano, M.A.; Riaguas, A.; Bernal, J.A. LIDENS: A program for lineament length and density analysis. *Comput. Geosci.* **2000**, *26*, 1011–1022. [[CrossRef](#)]
29. McElfresh, S.B.Z.; Harbert, W.; Ku, C.Y.; Lin, J.S. Stress modeling of tectonic blocks at Cape Kamchatka, Russia using principal stress proxies from high-resolution SAR: New evidence for the Komandorskiy block. *Tectonophysics* **2002**, *354*, 239–256. [[CrossRef](#)]
30. Aldharab, H.S.; Ali, S.A.; Ikbali, J.; Ghareb, S. GIS and hypsometry based analysis on the evolution of sub-basins in Ataq area-Shabwah, Yemen. *Int. J. Res. Appl. Sci. Eng. Technol.* **2018**, *6*, 3489–3497. [[CrossRef](#)]
31. Aldharab, H.S.; Ali, S.A.; Ikbali, J.; Ghareb, S.A. Spatial analysis of lineaments and their tectonic significance using Landsat imagery in Alarasa area-southeastern central Yemen. *J. Geogr. Environ. Earth Sci. Int.* **2018**, *18*, 1–13. [[CrossRef](#)]
32. Donoghue, D.; Thomas, M. *Remote Sensing and Image Interpretation*; Thomas, M., Ralph, W.K., Jonathan, C., Eds.; John Wiley: New York, NY, USA, 2000; p. 736.
33. Prasad, A.D.; Jain, K.; Gairola, A. Mapping of Lineaments and Knowledge Base Preparation using Geomatics Techniques for part of the Godavari and Tapi Basins, India: A Case Study. *Int. J. Comput. Appl.* **2013**, *70*, 39–47. [[CrossRef](#)]
34. Hardcastle, K.C. Photolineament factor: A new computer-aided method for remotely sensing the degree to which the bedrock is fractured. *Photogramm. Eng. Remote. Sens.* **1995**, *61*, 739–747.
35. Stockli, R.; Vermote, E.; Saleous, N.; Simmon, R.; Herring, D. *The Blue Marble Next Generation—A True Color Earth Dataset Including Seasonal Dynamics from Modis*; Dataset User's Manual; NASA Earth Observatory: Washington, DC, USA, 2005. [[CrossRef](#)]
36. Becker, J.; Sandwell, D.; Smith, W.; Braud, J.; Binder, B.; Depner, J. Global Bathymetry and Elevation Data at 30 Arc Seconds Resolution: SRTM30_PLUS. *Mar. Geod.* **2009**, *32*, 355–371. [[CrossRef](#)]
37. Beicip. *Structural Map of Jordan, Scale 1:5,000,000, Geological Mapping Division*; Natural Resources Authority: Amman, Jordan, 1981.
38. Alavi, M. Tectonic Map of the Middle East, Scale 1:5,000,000: Geological. *Surv. Iran.* **1991**.
39. Taymaz, T.; Jackson, J.; McKenzie, D. Active tectonics of the North and Central Aegean Sea. *Geophys. J. Int.* **1991**, *106*, 433–490. [[CrossRef](#)]
40. McClusky, S.; Balassanian, S.; Barka, A.; Demir, C.; Ergintav, S.; Georgiev, I.; Gurkan, O.; Hamburger, M.; Hurst, K.H.; Kahle, H.; et al. Global positioning system constraints on plate kinematics and dynamics in the eastern Mediterranean and Caucasus. *J. Geophys. Res.* **2000**, *105*, 5695–5719. [[CrossRef](#)]
41. Brew, G.E. Tectonic Evolution of Syria Interpreted from Integrated Geophysical and Geological Analysis. Ph.D. Thesis, Cornell University of New York, New York, NY, USA, 2001.
42. Ziegler, M.A. Late Permian to Holocene paleofacies evolution of the Arabian plate and its hydrocarbon occurrences. *GeoArabia* **2001**, *6*, 445–504.
43. Fox, J.E.; Ahlbrandt, T.S. *Petroleum Geology and Total Petroleum Systems of the Widiyan Basin and Interior Platform of Saudi Arabia and Iraq*; US Geological Survey, US Department of the Interior: Denver, CO, USA, 2002.
44. Diabat, A.; Masri, A. Orientation of the principal stresses along Zerqa-Ma'in Fault. *Mu'tah Lil-Buhuth Wad-Dirasat* **2005**, *20*, 57–71.
45. Dilek, Y. Eastern Mediterranean geodynamics. *Int. Geol. Rev.* **2010**, *52*, 111–116. [[CrossRef](#)]
46. Radaideh, O.M.A.; Melichar, R. Tectonic paleostress fields in the southwestern part of Jordan: New insights from the fault slip data in the southeastern flank of the Dead Sea Fault Zone. *Tectonics* **2015**, *34*, 1863–1891. [[CrossRef](#)]
47. Atallah, M. Tectonic evolution of northern Wadi Araba, Jordan. *Tectonophysics* **1992**, *204*, 17–26. [[CrossRef](#)]
48. Atallah, M. On the structural pattern of the Dead Sea Transform and its related structures in Jordan. *Abhath Al Yarmouk* **1992**, *1*, 127–143.
49. Chaimov, T.A.; Barzangi, M.; Al-Saad, D.; Sawaf, T.; Gebran, A. Mesozoic and Cenozoic deformation inferred from seismic stratigraphy in the southwestern intracontinental Palmyride fold-thrust belt, Syria. *Geol. Soc. Am. Bull.* **1992**, *104*, 704–715. [[CrossRef](#)]
50. Muneizel, S.S.; Khalil, B. The Geology of Al-Salt Map Sheet No. 3154–III. NRA. Internal report for the Natural Resources Authority, National Mapping Project. *Geol. Dir. Geol. Map. Div. Amman* **1993**.

51. Sawareih, A.; Barjous, M. The Geology of Suwaylih Map Sheet No. 3154-II. NRA. Internal report for the Natural Resources Authority, National Mapping Project. *Geol. Dir. Geol. Map. Div. Amman* **1993**.
52. Shawabkeh, K. The geology of Al Karama Area. Map Sheet No. 3153-IV, Internal report for the Natural Resources Authority, National Mapping Project. *Geol. Dir. Geol. Map. Div. Bulletin 57 Amman* **2001**.
53. Diabat, A.; Abdelghafoor, M. The Geology of Amman Map Sheet No. 3153-I. NRA. Internal report for the Natural Resources Authority, National Mapping Project. *Geol. Dir. Geol. Map. Div. Amman* **2004**.
54. Burdon, D.J. *Handbook of the Geology of Jordan: To Accompany and Explain the Three Sheets of the 1:250,000 Geological Map of Jordan East of the Rift by Albert M. Quennell*; Government of the Hashemite Kingdom of Jordan: Benham, UK, 1959.
55. Bender, F. *Geologie von Jordanien—Beiträge zur Regionalen Geologie der Erde*; 7 Gebrüder Borntraeger: Stuttgart, Germany, 1968.
56. Quennell, A.M. The Western Arabia rift system. *Geol. Soc. Lond. Spec. Publ.* **1984**, *17*, 775–788. [[CrossRef](#)]
57. Abed, A.M. On the genesis of the phosphorite—Chert association of the Amman formation in the Tel Es-Sur area, Ruseifa, Jordan. *Sci. Geol. Bull.* **1989**, *42*, 141–153. [[CrossRef](#)]
58. Atallah, M.; Mikbel, S.H. Structural analysis of the folds between Wadi El Yabis and the basalt plateau, northern Jordan. *Dirasat* **1992**, *19*, 43–58.
59. Sahawneh, J.; Atallah, M. Tectonic evolution of the north-eastern corner of the Dead Sea, Jordan. *Abhath Al Yarmouk* **2002**, *11*, 581–598.
60. Diabat, A. Structural and stress analysis based on fault-slip data in the Amman area, Jordan. *J. Afr. Earth Sci.* **2009**, *54*, 155–162. [[CrossRef](#)]
61. Langridge, R.M.; Ries, W.F.; Farrier, T.; Barth, N.C.; Khajavi, N.; De Pascale, G.P. Developing sub 5-m LiDAR DEMs for forested sections of the Alpine and Hope faults, South Island, New Zealand: Implications for structural interpretations. *J. Struct. Geol.* **2014**, *64*, 53–66. [[CrossRef](#)]
62. Radaideh, O.M.; Grasemann, B.; Melichar, R.; Mosar, J. Detection and analysis of morphotectonic features utilizing satellite remote sensing and GIS: An example in SW Jordan. *Geomorphology* **2016**, *275*, 58–79. [[CrossRef](#)]
63. Mark, R.K. *A Multidirectional, Oblique-Weighted, Shaded-Relief Image of the Island of Hawaii (No. 92-422)*; US Dept. of the Interior, US Geological Survey: Reston, VA, USA, 1992.
64. Juhari, M.A.; Ibrahim, A. Geological applications of Landsat TM imagery: Mapping and analysis of lineaments in NW Peninsula Malaysia. In Proceedings of the 18th Asia Conference on Remote Sensing, Kuala Lumpur, Malaysia, 20–24 October 1997; pp. J-1-1–J-1-8.
65. Akman, A.Ü.; Tüfekci, K. Determination and characterization of fault systems and geomorphological features by RS and GIS techniques in the WSW part of Turkey. In Proceedings of the 20th ISPRS Congress, Istanbul, Turkey, 12–23 July 2004; pp. 899–904.
66. Micheal, W.F.P.G. *Lineaments Analysis South Florida Region, Aquifer Storage and Recovery Regional Study*; Draft Technical Memorandum, Central and Southern Florida Project; Army Corps of Engineers: Jacksonville, FL, USA, 2004.
67. Walker, R.T. Remote Sensing study of active folding and faulting in southern Kerman province, southeast Iran. *J. Struct. Geol.* **2006**, *28*, 654–668. [[CrossRef](#)]
68. Freund, R. A model of the structural development of Israel and adjacent areas since Upper Cretaceous times. *Geol. Mag.* **1965**, *102*, 189–205. [[CrossRef](#)]
69. Wilson, J.T. A new class of faults and their bearing on continental drift. *Nature* **1965**, *207*, 343–347. [[CrossRef](#)]
70. Larsen, B.; Ben-Avraham, Z.; Shulman, H. Fault and salt tectonics in the southern Dead Sea basin. *Tectonophysics* **2002**, *346*, 71–90. [[CrossRef](#)]
71. Mahmoud, Y.; Masson, F.; Meghraoul, M.; Cakir, Z.; Alchalbi, A.; Yavaoglu, H.; Yönlü, O.; Daoud, M.; Ergintav, S.; Inan, S. Kinematic study at the junction of the East Anatolian fault and the Dead Sea fault from GPS measurements. *J. Geodyn.* **2013**, *67*, 30–39. [[CrossRef](#)]
72. Garfunkel, Z.; Zak, I.; Freund, R. Active faulting in the Dead Sea rift. The Dead Sea Rift. *Tectonophysics* **1981**, *80*, 1–26. [[CrossRef](#)]
73. Girdler, R. The Dead Sea transform system. *Tectonophysics* **1990**, *180*, 1–13. [[CrossRef](#)]
74. Alchalbi, A.; Daoud, M.; Gomez, F.; McClusky, S.; Reilinger, R.; Abu Romeyeh, M.; Alsouod, A.; Yassminh, A.; Ballani, B.; Darawcheh, R.; et al. Crustal deformation in northwestern Arabia from GPS measurements in Syria: Slow slip rate along the northern Dead Sea Fault. *Geophys. J. Int.* **2010**, *180*, 125–135. [[CrossRef](#)]

75. Bosworth, W.; Huchon, P.; McClay, J. The Red Sea and Gulf of Aden Basins. *J. Afr. Earth Sci.* **2005**, *43*, 334–378. [[CrossRef](#)]
76. Quennell, A.M. Evolution of the Dead Sea Rift. In *Proceedings of the 1st Jordan Geological Conference: Amman, Jordan*; Abed, A.M., Khaled, H.M., Eds.; The University of Jordan: Amman, Jordan, 1983; pp. 460–482.
77. Al-Tawalbeh, M.; Atallah, M.; Al Tamimi, M. Structural Evolution of the Area North of Ajloun Dome, Jordan. *Jordan J. Earth Environ. Sci.* **2017**, *8*, 55–60.
78. Abutaha, S.; Atallah, M.; Abed, A.M. Structural Evolution of Wadi Hudaydun in Wadi Shueib Area, NW Jordan. *Jordan J. Earth Environ. Sci.* **2019**, *10*, 152–160.
79. Salameh, E.; Zacher, W. Horizontal stylonites and paleostress in Jordan. *Neues Jahrbuch für Geologie und Paläontologie. Monatshefte* **1982**, *8*, 509–512.
80. Diabat, A. Paleostress and strain analysis of the Cretaceous Rocks in the Eastern Margin of the Dead Sea Transform, Jordan. Ph.D. Thesis, Baghdad University, Baghdad, Iraq, 1999.
81. Diabat, A. Strain analysis of the Cretaceous rocks in the Eastern margin of the Dead Sea Transform, Jordan. *Dirasat* **2002**, *29*, 159–172.
82. Diabat, A. The state of paleostress along the Siwaqa fault based on fault-slip data. *Al Manarah* **2006**, *12*, 131–150.
83. Zain Eldeen, U.; Delvaux, D.; Jacobs, P. Tectonic evolution in the Wadi Araba Segment of the Dead Sea Rift, Southwest Jordan. *EGU Stephan Mueller Spec. Publ. Ser.* **2002**, *2*, 63–81. [[CrossRef](#)]
84. Diabat, A.; Salih, M.; Atallah, M. Magnitudes of the paleostresses at the Eastern Rim of the Dead Sea Transform Fault, Jordan. *Dirasat* **2003**, *30*, 1–18.
85. Alhejoj, I.; Alqudah, M.; Alzughoul, K.; Tarawneh, A. Post-Cretaceous Mesosstructures and Their Formation Mechanisms, Jordan. *Jordanian J. Earth Environ. Sci.* **2019**, *9*, 116–126.
86. Joffe, S.; Garfunkel, Z. Plate kinematics of the circum Red Sea. A re-evaluation. *Tectonophysics* **1987**, *141*, 5–22. [[CrossRef](#)]
87. Chu, D.; Gordon, R.G. Current plate motions across the Red Sea. *Geophys. J. Int.* **1998**, *135*, 313–328. [[CrossRef](#)]
88. Zak, I.; Freund, R. Recent strike-slip movement along the Dead Sea Rift. *Isr. J. Earth Sci.* **1966**, *15*, 33–37.
89. Freund, R.; Zak, I.; Garfunkel, Z. Age and rate of the sinistral movement along the Dead Sea rift. *Nature* **1968**, *220*, 253–255. [[CrossRef](#)]
90. McKenzie, D.; Davies, D.; Molnar, P. Plate tectonics of the Red Sea and East Africa. *Nature* **1970**, *226*, 243–248. [[CrossRef](#)] [[PubMed](#)]
91. Ben-Avraham, Z.; Almagor, G.; Garfunkel, Z. Sediments and structures of the Gulf of Elat (Aqaba)—Northern Red Sea. *Sediment. Geol.* **1979**, *23*, 239–267. [[CrossRef](#)]
92. Shapira, A.; Hofstetter, H. Source parameters and scaling relationships of earthquakes in Israel. *Tectonophysics* **1993**, *217*, 217–226. [[CrossRef](#)]
93. Klinger, Y.; Avouac, J.P.; AbouKarak, N.; Dorbath, L.; Bourles, D.; Reyss, J.L. Slip-rate on the Dead Sea transform fault in northern Araba valley. *Geophys. J. Int.* **2000**, *142*, 755–768. [[CrossRef](#)]
94. Klinger, Y.; Avouac, J.P.; Dorbath, C.; Abou Karaki, N.; Tisnerat, N. Seismic behavior of the Dead Sea fault along Araba valley, Jordan. *Geophys. J. Int.* **2000**, *142*, 769–782. [[CrossRef](#)]
95. Meghraoui, M. Paleoseismic History of the Dead Sea Fault Zone. In *Encyclopedia of Earthquake Engineering*; Springer: Berlin/Heidelberg, Germany, 2015. [[CrossRef](#)]
96. Niemi, T.; Zhang, H.; Atallah, M.; Harrison, J. Late Pleistocene and Holocene slip-rate of the northern Wadi Araba fault, Dead Sea transform, Jordan. *J. Seismol.* **2001**, *5*, 449–474. [[CrossRef](#)]
97. Ferry, M.; Meghraoui, M.; Abu Karaki, N.; Al-Taj, M.; Amoush, H.; Al-Dhaisat, S.Y.; Barjous, M. A 48-kyr-long slip rate history for the Jordan Valley segment of the Dead Sea Fault. *Earth Planet. Sci. Lett.* **2007**, *260*, 394–406. [[CrossRef](#)]
98. Bender, F. *Geology of the Arabian Peninsula (Jordan)*; US Geological Survey: Reston, VA, USA, 1975.
99. Powell, J.H. Stratigraphy and sedimentation of the Phanerozoic rocks in central and southern Jordan. Part B: Kurnub, Ajlun, and Belqa groups. Natural Resources Authority. *Geol. Dir. Geol. Map. Div.* **1989**, *11*, 130.
100. Powell, J.H.; Moh'd, B.K. Evolution of Cretaceous to Eocene alluvial and carbonate platform sequences in central and south Jordan. *GeoArabia* **2011**, *16*, 29–82.
101. Abed, A.M. *Geology of Jordan. It's Environment and Water*; Scientific Series 1; Publication of Association of Jordanian Geologists: Arabic, Jordan, 2000; p. 571.

102. Al-Taj, M.M. Active faulting along the Jordan Valley segment of the Jordan–Dead Sea Transform. Ph.D. Thesis, University of Jordan, Amman, Jordan, 2000.
103. Environmental Systems Research Institute (Esri, ArcGIS®10.7). 2019. Available online: <http://www.esri.com> (accessed on 8 December 2019).
104. Sabins, F.F. *Remote Sensing: Principles and Interpretation*, 3rd ed.; W.H. Freeman and Company: New York, NY, USA, 1996; p. 494.
105. PCI Geomatics. Geomatica Online Help. 2018. Available online: <http://www.pcigeomatics.com/geomatica-help/> (accessed on 20 August 2019).
106. Hung, L.Q.; Dinh, N.Q.; Batelaan, O.; Tam, V.T.; Lagrou, D. Remote sensing and GIS-based analysis of cave development in the Suoimuoi Catchment (Son La—NW Vietnam). *J. Cave Karst Stud.* **2002**, *64*, 23–33.
107. RockWare Geoscientific Software. Online Help. Available online: <https://www.rockware.com/> (accessed on 1 July 2019).
108. Chopra, S. Interpreting fractures through 3D seismic discontinuity attributes and their visualization. *CSEG Recorder* **2009**, *34*, 5–14.
109. Pinheiro, M.R.; Cianfarra, P.; Salvini, F. Tectonics of the Northeastern border of the Parana Basin (Southeastern Brazil) revealed by lineament domain analysis. *J. S. Am. Earth Sci.* **2019**, *94*, 102231. [[CrossRef](#)]
110. Wise, D.U.; Funicello, R.; Parotto, M.; Salvini, F. Topographic lineament swarms: Clues to their origin from domain analysis of Italy. *Geol. Soc. Am. Bull.* **1985**, *96*, 952–967. [[CrossRef](#)]
111. Al-Awabdeha, M.; Pérez-Peñaab, J.V.; Azañónac, J.M.; Booth-Reaac, G.; Abed, A.; Atallah, M.; Galvea, J.P. Stress analysis of NW Jordan: New episode of tectonic rejuvenation related to the Dead Sea transform fault. *Arab. J. Geosci.* **2016**, *9*, 264. [[CrossRef](#)]
112. Palano, M.; Imprescia, P.; Gresta, S. Current stress and strain-rate fields across the Dead Sea Fault System: Constraints from seismological data and GPS observations. *Earth Planet. Sc. Lett.* **2013**, *369*, 305–316. [[CrossRef](#)]
113. Cianfarra, P.; Maggi, M. Cenozoic extension along the reactivated Aurora Fault System in the East Antarctic Craton. *Tectonophysics* **2017**, *703*, 135–143. [[CrossRef](#)]
114. Carreras, J. Zooming on Northern Cap de Creus shear zones. *J. Struct. Geol.* **2001**, *23*, 1457–1486. [[CrossRef](#)]
115. Cunningham, W.D.; Mann, P. *Tectonics of Strike-Slip Restraining and Releasing Bends*; Geological Society: London, UK; Special Publications: London, UK, 2007; Volume 290, pp. 1–12.
116. Mansoor, N. A GIS-Based Assessment of Active Faults and Liquefaction Potential of the City of Aqaba, Jordan. Master’s Thesis, UMKC, Kansas, MO, USA, 2002.
117. Mansoor, N.; Niemi, T.; Misra, A. A GIS-based assessment of the liquefaction potential of the city of Aqaba, Jordan. *Environ. Eng. Geosci.* **2004**, *10*, 297–320. [[CrossRef](#)]
118. Bowman, D.; King, G.; Tapponnier, P. Slip Partitioning by Elastoplastic Propagation of Oblique Slip at Depth. *Science* **2003**, *300*, 1121–1123. [[CrossRef](#)]
119. Jones, R.; Tanner, P. Strain partitioning in transpression zones. *J. Struct. Geol.* **1995**, *17*, 793–802. [[CrossRef](#)]
120. Gomez, F.; Nemer, T.; Tabet, C.; Khawlie, M.; Meghraoui, M.; Barazangi, M. *Restraining Bend of the Dead Sea Fault (Lebanon and SW Syria) Strain Partitioning of Active Transpression within the Lebanese*; Geological Society: London, UK; Special Publications: London, UK, 2007; Volume 290, pp. 285–303.

